PAPER

Check for updates

Frontier performance of *in situ* formed α-MnO$_2$ dispersed over functionalized multi-walled carbon nanotubes covalently anchored to a graphene oxide nanosheet framework as supercapacitor materials†

Md. Mahinur Islam, [ID] M. Yousuf Ali Mollah, Md. Abu Bin Hasan Susan [ID] and Md. Mominul Islam [ID]*

α-MnO$_2$ has been recognized as a potential material for supercapacitor applications because of its abundance, cost-effectiveness, environmental-benign nature and high theoretical specific capacitance (C_{sp}) of 1370 F g^{-1}. In this study, we succeeded for the first time to achieve the theoretical C_{sp} with 3D multi-walled carbon nanotubes (MWCNTs) horizontally dispersed on 2D graphene oxide (GO) nanosheet framework-supported MnO$_2$ ternary nanocomposites synthesized by a simple precipitation method. The *in situ* formation of α-MnO$_2$ and GO, and the growth of 3D MWCNT/GO framework took place simultaneously in a strong acidic suspension containing functionalized-MWCNTs, graphite, NaNO$_3$ and KMnO$_4$. Characterizations of the composites synthesized by varying % wt MWCNTs were performed with state-of-the-art techniques. These composites were characterized to be semi-crystalline and mesoporous in nature, and the scrupulous analyses of field emission scanning electron microscopic images showed MnO$_2$ nano-flower distributed over 3D MWCNTs dispersed-on-GO-nanosheet frameworks. These composites deposited on a graphite electrode exhibited an ideal supercapacitive behavior in an Na$_2$SO$_4$ solution measured *via* cyclic voltammetry and chronopotentiometry. Optimum contents of MnO$_2$ and MWCNTs in the composites showed a maximum C_{sp} of 1380 F g^{-1} with satisfactory energy and power densities compared in the Ragone plot. An ascending trend of C_{sp} against the charge–discharge cycle number studied for 700 cycles was noticed. Well-dispersion of α-MnO$_2$ nanoparticles throughout 3D MWCNTs covalently-anchored to the GO nanosheet framework is discussed to aid in achieving the frontier C_{sp} of MnO$_2$.

1. Introduction

In the past decades, the ascending demands of electrical energy for modern smart appliances have attracted considerable attention of the alternative energy storage devices such as lithium-ion batteries, capacitors and supercapacitors.[1–4] Supercapacitors have been considered as the most promising energy storage protocol due to their superior specific capacitance (C_{sp}), high power density and outstanding stability in applications.[2–4] Micro-structures of metal oxides such as MnO$_2$,[5,6] RuO$_2$,[7] NiO,[8] and Co$_3$O$_4$,[9] and their hybrids[10,11] have been recognized as promising supercapacitor materials. MnO$_2$ is an environmentally friendly, inexpensive and abundant transition metal oxide, and its various allotropes have been used as molecular sieves,

Department of Chemistry, Faculty of Science, University of Dhaka, Dhaka 1000, Bangladesh. E-mail: mominul@du.ac.bd

† Electronic supplementary information (ESI) available. See DOI: 10.1039/d0ra08772f

catalysts and electrode materials in dry cell batteries in addition to supercapacitor applications.[4,12]

The high prospect of the α form of MnO$_2$ in designing supercapacitor electrodes has been focused because of its high theoretical C_{sp} of 1370 F g^{-1}.[13] The experimentalists in this field are in a kind of race to reach this milestone of theoretical C_{sp} by attempting to tune the morphology of MnO$_2$ using mainly carbonaceous and polymeric frameworks. Accordingly, huge numbers of research works have been published in recent years on this focal issue.[14,15] The research work on MnO$_2$ as a supercapacitor material has been launched from the work of Lee and John in 1999.[16] The amorphous MnO$_2$·H$_2$O has been reported to show a C_{sp} of 200 F g^{-1} in an aqueous KCl solution.[16] Later on Liu *et al.* achieved a C_{sp} of 379 F g^{-1} by tuning the morphology of MnO$_2$ to form a bowl-like nanosheet with an ultra-thin thickness (*ca.* 4 nm) synthesized by a template-assisted hydrothermal method.[15] Wang *et al.* have shown the influence of electrolytic media on the C_{sp} of Mn$_3$O$_4$-embedded-graphene composite to be 175 F g^{-1} in 1.0 M Na$_2$SO$_4$ and 256 F g^{-1} in

6.0 M KOH solutions.[17] It has been revealed that C_{sp} decreases drastically as the thickness of the MnO_2 film increases.[13] This is reasonable since the underlying part of the nonporous material would not play the role in the charging-discharging cycle to contribute to C_{sp}.

Recently, Huang *et al.* have pointed out several crucial points in fostering C_{sp} of materials including the use of highly conductive, porous and conductive polymeric materials as the dispersing matrix.[15] The researchers have succeeded to some extent by following these routes in designing efficient MnO_2 composites with different frameworks to enhance C_{sp} to, *e.g.*, 242 F g^{-1} with MnO_2/polyaniline (PAni) composites,[18] 300 F g^{-1} with an *in situ* electrodeposited PAni/MnO_2 composite,[19] 395 F g^{-1} with MnO_2/PAni/multi-walled carbon nanotubes (MWCNTs) composites,[20] 646 F g^{-1} with stalagmite MnO_2 nanorod arrays growing vertically on flexible Ni substrates,[21] 752 mA h g^{-1} with MnO_2–graphene having a sandwich structure[22] and 964 F g^{-1} with multi-layered graphene/CNTs/MnO_2 nanocomposite interconnected pore networks.[23] As far as we reviewed, the study by Jia *et al.* is the latest, wherein the highest C_{sp} of MnO_2 of 1229 F g^{-1} has been achieved by creating a special tube-on-sheet architecture of the meso-structured composite of CNT-on-MnO_2 nanosheets of which the CNTs are vertically aligned on porous MnO_2 nanosheets.[24] This study has in fact motivated us in using MWCNTs covalently fixed on graphene oxide (GO) nanosheets as the dispersing agents for MnO_2.

MWCNTs is an attractive material used in numerous applications including as a filler owing to its good electrical conductivity, high surface area, mechanical strength, chemical stability and low mass density.[25,26] MWCNT itself does not meet the requirements for a commercial storage devices due to its low C_{sp} only of 58 F g^{-1}.[27] The low C_{sp} probably arises from the high aggregation of MWCNTs *via* strong hydrophobic forces that results in a poor exposure of the active site to the electrolytes.[26,28] On the other hand, GO is a 2D material derived from graphite by introducing covalent C–O bonds first reported in 1855.[29] Due to its ability to remain exfoliated in water as single atomic-layered sheets, cast as films, and be further reduced back to graphene, GO has been used in numerous applications as conductive films, electrode materials and composites.[29]

In this study, we successfully synthesized efficient ternary composites of MnO_2/MWCNTs/GO by following basically two-fold molecular engineering as: (i) the dispersion of MWCNTs *via* the formation of an ester-like bond between the –COOH group of functionalized MWCNTs and the –OH group of GO and (ii) the dispersion of *in situ* formed nanoparticles of MnO_2 *via* a precipitation method over the MWCNT/GO matrix formed simultaneously. Prior to the formation of composites, the introduction of the –COOH group on the MWCNT surface was carried out by a strong acid treatment.[30] Binary composites of MnO_2/GO were also prepared. The as-prepared composites were characterized with Fourier-transform infrared (FTIR) spectroscopy, field emission scanning electron microscopy (FESEM), energy dispersive X-ray spectroscopy (EDS), X-ray diffraction (XRD) and Brunauer–Emmett–Teller (BET) surface analysis techniques. The storage characteristics of the composites deposited on graphite electrodes were evaluated *via* cyclic voltammetry and galvanostatic charge–discharge (GCD) measurements.

2. Experimental

2.1 Chemicals and materials

Analytical-grade chemicals and materials such as potassium bromide, KBr (Sigma, Germany), graphite powder (purity: 99.975% carbon basis, particle size: <20 μm, Sigma-Aldrich, Switzerland), sodium nitrate, $NaNO_3$ (Merck, Germany), potassium permanganate, $KMnO_4$ (JAM, Germany), sulphuric acid, H_2SO_4 (Merck, Germany), hydrochloric acid, HCl (RCI, Thailand), sodium sulphate, Na_2SO_4 (BDH, England), MWCNTs (Sigma-Aldrich, USA), nitric acid, HNO_3 (Merck, India) and poly(vinylidine fluoride), PVDF (Sigma-Aldrich, Germany) were used without any further purification. Ultrapure water (specific conductance <0.1 μS cm^{-1}) prepared by using BOECO pure (Model-BOE 8082060, Germany) was used in this study. A graphite rod (diameter: 6.15 mm, purity: 99.99%) was purchased from Alfa Aesar, USA.

2.2 Functionalization of MWCNTs

The commercial MWCNTs exist as agglomerates of several hundred micrometers.[31] To segregate these MWCNT fibrils, a chemical treatment was carried out in an acidic solution. Typically, 300 mg of MWCNTs were first ultrasonicated in deionized water for 4 h to ensure their dispersion. The sonication was continued for 5 h more by adding a mixture of concentrated H_2SO_4 (95%) and HNO_3 (65%) at a ratio of 3 : 1. The mixture was then allowed to settle down and then filtered using a double ring filter paper. The solid mass was washed with deionized water until the pH of the filtrate was *ca.* 7.[32] The thus-functionalized MWCNTs, named as F-MWCNT, were used as a precursor for the synthesis of the ternary composites under consideration.

2.3 *In situ* synthesis of 3D MnO_2/MWCNT/GO composites

The ternary composites studied were synthesized *via* a chemical method,[33] wherein the formation of α-MnO_2 and GO as well as the formation of a 3D MWCNT/GO framework through the reaction between –OH groups of nascent GO and –COOH groups of F-MWCNT that occurred simultaneously. Typically, about 0.10 g of graphite powder as the source of GO, 0.05 g of $NaNO_3$ and 0.015 g of F-MWCNT were mixed in 20 mL of 95% H_2SO_4 and the suspension was kept under a constant stirring in an ice bath. Then, 0.40 g of solid $KMnO_4$ was gradually added to the suspension. After the addition of $KMnO_4$, stirring was continued at 30 °C, room temperature, for 2 h. The colour of the suspension became bright brown. This brown suspension was heated, followed by an addition of 90 mL deionized water to quickly raise the temperature to *ca.* 100 °C. Finally, the brown suspension turned to black that was allowed to settle down overnight. After filtering out, the collected black solid mass was washed several times with deionized water to remove soluble ions. The desired product dried under vacuum was obtained as a black powder. The % weight F-MWCNT feed was 15, and the

composite was named as GMCNT-15. Similarly, five composites were synthesized by varying the % weight F-MWCNT feed, as summarized in Table 1. The methods for the preparation of binary composites of MnO$_2$/GO are described in ESI.†

2.4 Characterizations of the materials

The morphology, structure and chemical stability of the sample were studied *via* FE-SEM (JSM-7600F, JEOL, USA) using an FTIR spectrometer (Frontier FT-NIR/MIR, Perkin Elmer, USA). Surface area, pore volume and pore diameter of the as-prepared samples were analysed by N$_2$ gas adsorption–desorption *via* the BET method using a BET surface analyser (Belsorpmini-II, BEL, Japan). Phase analysis and chemical characterization of the samples were carried out *via* XRD (Philips PW 1724) X-ray generator using an XDC-700 Guinier-Hagg focusing camera with strictly monochromatized CuKα radiation ($\lambda = 1.540598$).

2.5 Electrochemical measurements

A single compartment, threeelectrode cell was used for electrochemical measurements, where the data were recorded using a computer-controlled electrochemical analyser system (Model: CHI 760E, USA). The electrochemical measurements in 0.5 M Na$_2$SO$_4$ electrolytic solutions were conducted using a modified graphite electrode as the working electrode, a spiral Pt wire and silver|silver chloride|saturated KCl solution [Ag|AgCl|KCl(sat.)] electrode as counter and reference electrodes, respectively. Cyclic voltammograms (CVs) were recorded in the potential range of 0.1–0.8 V at different scan rates (v). GCD curves were recorded in the same potential range using different current densities.

3. Results and discussion

3.1 Functionalization of MWCNTs and syntheses of composites

The functionalization of MWCNTs to introduce –COOH and –OH groups on the surface was carried out in a strong acidic solution comprising a mixture of concentrated H$_2$SO$_4$ and HNO$_3$.[31] Black powder of functionalized MWCNTs, *i.e.*, F-MWCNT was formed *via* the esterification reaction (ESI†). The
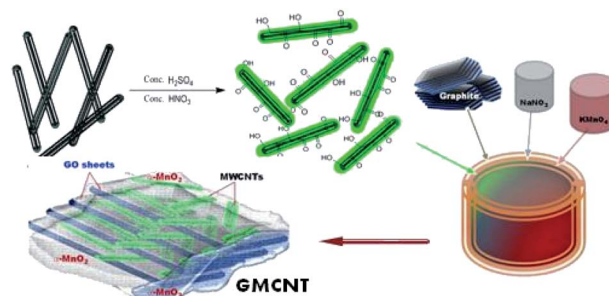
Scheme 1 Formation of GMCNT composites.

stability of the dispersion of F-MWCNT has been considered as an indirect measure of the degree of functionalization of MWCNTs.[34] Accordingly, this was corroborated by dispersing the as-prepared F-MWCNT in water, followed by sonication for 10 min.

It formed a long-standing dispersion. The thus-formed negatively charged –COOH group would repeal each other and did not allow the MWCNTs to aggregate, as in the case of pristine ones. The chemical reaction involving the formation of the ternary composite of 3D MWCNT-top-on-GO nanosheet frameworks is expressed in ESI.† The *in situ* formation of α-MnO$_2$ and GO, and the growth of the 3D MWCNT/GO framework through the reaction between –OH groups of nascent GO formed instantly and –COOH groups of F-MWCNT added in a suspension containing graphite, NaNO$_3$ and KMnO$_4$ occur simultaneously under strong acidic conditions (Scheme 1). The binary composite of MnO$_2$/GO was prepared in the absence of F-MWCNT.[32] These materials were subjected to relevant characterizations and used to modify graphite electrodes used as supercapacitor electrodes.

The introduction of –COOH groups on MWCNT surfaces was successful as confirmed by FTIR spectral analyses (Fig. 1a). The two characteristic bands at 1720 and 2350 cm^{-1} are associated with the stretching vibrations of >C=O and O–C=O groups, respectively, of the –COOH group.[35–37] The bands at 1410 and 1227 cm^{-1} correspond to the O–H deformation and stretching vibration of C–O, respectively, confirming the presence of the epoxy group.[38] A strong, broad band at 1590 cm^{-1} for the

Table 1 Materials synthesized/functionalized and the summary of the results of their BET characterizations

Materials synthesized/ treated[a]	Abbreviated name	% MnO$_2$ content[b]	BET characterizations			
			Surface area (m^2 g^{-1})	Pore diameter (nm)	Mean pore diameter (nm)	Total pore volume (cm^3 g^{-1})
Graphene oxide	GO	—	—	—	—	—
GO/MnO$_2$	GOM	2.50	4	1.48	4	0.004
Functionalized MWCNT	F-MWCNT	—	105	37.03	50	1.315
5% MWCNT + GO/MnO$_2$	GMCNT-5	0.52	7	1.86	12	0.035
10% MWCNT + GO/MnO$_2$	GMCNT-10	—	15	2.12	19	0.045
15% MWCNT + GO/MnO$_2$	GMCNT-15	0.75	14	2.55	24	0.085
30% MWCNT + GO/MnO$_2$	GMCNT-30	0.65	12	2.20	20	0.056
50% MWCNT + GO/MnO$_2$	GMCNT-50	0.15	7	2.29	14	0.025

[a] % represents feed amount of MWCNT. [b] Determined with EDS.
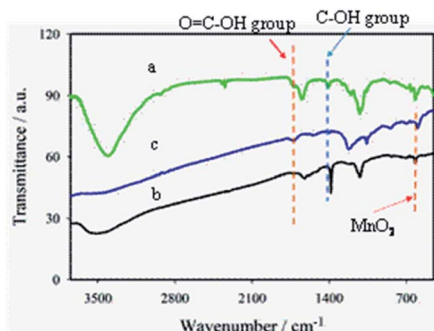
Fig. 1 Typical FTIR spectra of (a) F-MWCNT, (b) GOM and (c) GMCNT-15.

Fig. 2 FESEM images of (a) GOM, (b) F-MWCNT, (c) GMCNT-15, (d) GMCNT-30 and (e) GMCNT-50, and (f) typical EDS spectrum of GMCNT-15.

aromatic C=C group, confirms the presence of sp^2 hybridized carbon in GO (Fig. 1b).[38] Moreover, a sharp peak at 615 cm^{-1} for Mn–O vibration[39,40] with the characteristic epoxy bands at 1405 and 1250 cm^{-1} for GO were also observed. The weak band at 1060 cm^{-1} indicates the C–OH stretching vibration of the alkoxy group for GOM composites.[41–43] Thus, these oxygen-containing functional groups indicate that the graphite is oxidized to form GO.[44]

In the FTIR response typically shown for GMCNT-15, several characteristics features are noticed: (i) the blue shifts of >C=O (1728 cm^{-1}) and the alkoxy C–OH (1076 cm^{-1}) group of F-MWCNT, (ii) diminishing of the bands around 3450, 1450 and 1250 cm^{-1} associated with O–H vibration, O–H deformation, C–O epoxy stretching of chemisorbed water, respectively.[38] The observed blue-shift of the band of the >C=O group confirms the formation of an ester-linkage in the composite.[45] The decrease in the intensity of the broad band between 3600 and 3000 cm^{-1} is indicative of the removal of chemisorbed water in GMCNT-15 through H-bonding as the O=C–O bond is formed.[38] The possibility of these reactions can be further supported by the studies of Jorden *et al.* and Luckhaus *et al.*, where hydrogen-bonding interactions between GO and with F-MWCNT have been modelled theoretically.[46,47] The extent of interactions depends on the efficiency of the insertion of F-MWCNT between the GO sheets during the *in situ* exfoliation process, best achieved at 15% of F-MWCNT. Thus, the –COOH group of F-MWCNT reacts with the –OH group of GO to form an ester-like linkage in this acidic environment.[45] The FTIR spectra of other GMCNT composites are described in ESI.†

In the typical EDS response of GMCNT-15 (Fig. 2f), the characteristic peaks of Mn, C and O elements were observed. The % mass of these elements were determined by spotting on three distinct positions of the FESEM image. Similar studies for all binary and ternary composites were carried out and the values of % MnO$_2$ are summarized in Table 1. The % MnO$_2$ in GOM is 2.50, *i.e.*, GOM contains about 97% of C and O species as GO. In general, the ternary composites contain a small amount of MnO$_2$, among which GMCNT-15 contains the highest % MnO$_2$ of 0.75. The growth of MnO$_2$ would simultaneously take place on the surface of GO and MWCNT and inside the pores of MWCNTs, *i.e.*, *in situ* formed MnO$_2$ fills the tube of
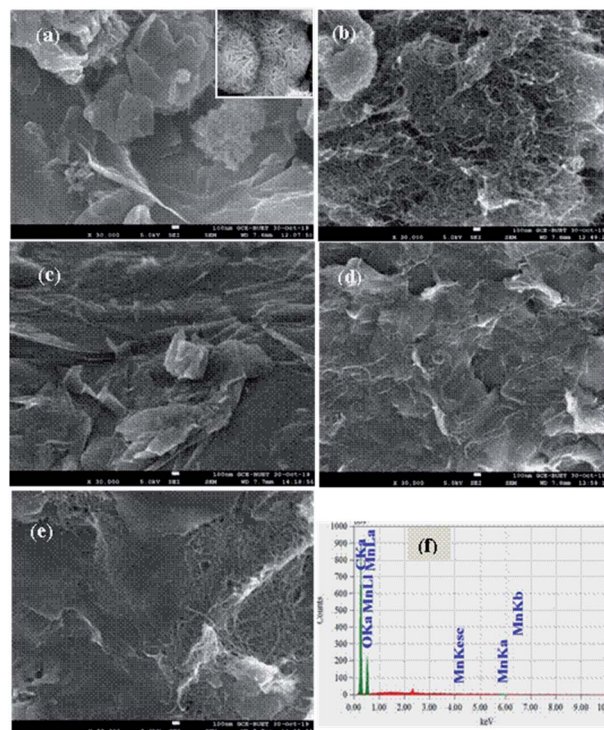
MWCNTs. Although it is not clear, the underlying MnO$_2$ in the ternary composite including MWCNT-30 and MWCNT-50 may not be exposed for detection with EDS. Consequently, the amount of MnO$_2$ loading was observed to decrease upon increasing the amount of MWCNTs in the ternary composite.

Fig. 2 illustrates FESEM images of the as-prepared materials. In the low magnification image of the GOM composite, GO nanosheets are found to be curly separated with a number amount of MnO$_2$ nanoparticles densely deposited on their layer. The high magnification FESEM image shown in the inset clearly shows the nano-flower morphology of MnO$_2$ particles (Fig. 2a). The FESEM image of F-MWCNT shows that MWCNTs are highly coagulated and bundled, whereas F-MWCNTs are distributed quite uniformly and MnO$_2$ are dispersed on MWCNT and GO sheet in GMCNT-15. MWCNTs were found to reform aggregates in GMCNT-50 as in the case of F-MWCNT. The particle size distribution with the particle count of all GMCNTs, which were statistically evaluated by measuring the diameters of 100 randomly picked nanoparticles is shown in ESI.† GMCNT-15 has the highest particle counts with an average size of 10.30 nm. In GMCNT-50, there is a significant reduction in the particle count with a simultaneous increase in the average area of the particles. From these observations, it can be inferred that the functionalization of MWCNT is an effective method for preventing their agglomeration, and GO-assisted well-dispersion of MWCNTs up to their certain compositions and *in situ* formed MnO$_2$ particles are uniformly distributed over the

binary bed of the MWCNT/GO framework in the ternary composites.

Fig. 3 represents the XRD patterns of the GMCNT composites. The sharp peak at 2θ of 26.0° is a characteristic of the (002) plane of MWCNTs.[48] The characteristic peak of GO was found at $2\theta = 11.9°$ with an interlayer distance of 0.83 nm.[43] The peaks observed at 42.3 and 56.4° with a low intensity correspond to the (101) and (201) planes of α-MnO_2.[21,49] A decrease in the intensity is observed and the peak becomes broader as the amount of MWCNTs increases. It is worth mentioning that the shape, size and crystal planes of crystallite affect the shape of diffraction patterns (for details see ESI†). However, the crystallinity of GMCNT-5 was determined to be 90% with 13.5 nm single crystal of MWCNTs. Their degree of crystallinity and the size of crystallite decreased to become amorphous with a decrease in the feed amount of F-MWCNTs (see Table SI-1†). Most remarkably, the GMCNT-15 composite is only 17% crystalline with the crystallite size of 0.22 nm. The amorphous parts of the composite that has been reported to favour the electrolyte to insert into or to expel out from the matrix[50] during the charge–discharge cycle are beneficial to increase C_{sp} (*vide infra*).

As shown in Fig. SI-5,† the experimental XRD patterns of the sample matched well with the stimulated pattern of the triclinic crystal system with the P1 space group. The microstructure of the composite exhibits patterns of the oxide layer with Mn and C bridge adjacent layer into 3D architectures (Fig. SI-6†).[51] Thus, the as-synthesized 3D architectures are entirely made up of randomly oriented and entangled MWCNTs with amorphous GO and *in situ* formed α-MnO_2, as depicted in Scheme 1. Multi-covalent junctions of MWCNT such as Y-junctions were found within the entangled network structure.[52] The MWCNT interlinked with GO and *in situ* MnO_2 *via* esterification by the epoxy matrix formation in the presence of a strong acid,[31,53] which can be confirmed by the degree of dispersion.

The N_2 gas adsorption–desorption isotherms of the composites are shown in Fig. 4. The hysteresis loop is similar to the H3 type of mesoporous materials.[45,54] The BJH plots exhibit the distribution of the pore diameter. The surface parameters determined for all materials are summarized in Table 1. F-MWCNTs naturally possesses a high surface area of 105 m^2 g^{-1} with a large pore diameter of 37 nm. Both surface area and pore diameter of MWCNTs anchored to GO nanosheets significantly decreased in the presence of MnO_2 due to the disperson of MnO_2 occurring not only on the surface but also inside the
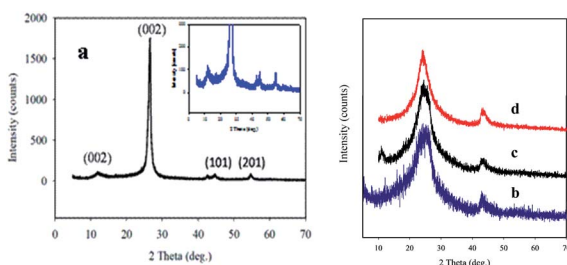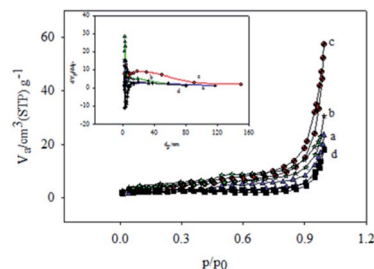

Fig. 4 Nitrogen adsorption–desorption isotherms of (a) GMCNT-5, (b) GMCNT-10, (c) GMCNT-15 and (d) GMCNT-50 composites. Inset represents corresponding BJH plots.

pores of MWCNT. It is interesting to note that when *in situ* formed MnO_2 in the GMCNT composites was maximum the surface and pore diameter became maximum (see Table 1). For GMCNT-15, *i.e.*, at the optimum composition of MWCNTs and MnO_2, the pore diameter was maximum, which is important for the charging-discharging of a material (*vide infra*).

3.2. Charge storage performances of the composites

To identify the non-faradaic zone in the CVs measured with the as-synthesized material modified-graphite electrodes, the CV scan was initially performed in the potential range of 0.0–1.2 V (Fig. 5A). In the potential range of 0.1–0.8 V, an almost symmetric rectangular shape (box-shaped) response, characteristic of a non-faradaic process,[55] was obtained. The shapes of CVs do not significantly change with the increase in v from 1 to 100 mV s^{-1} (Fig. 5B), suggesting that the materials showed an ideal capacitive behaviour at a higher rate of charge–discharge capabilities.[55] Similar studies for F-MWCNTs and GOM were also carried out as compared with GMCNT-15 (Fig. 5C). Besides other features, the currents of the CVs for GO and F-MWCNTs
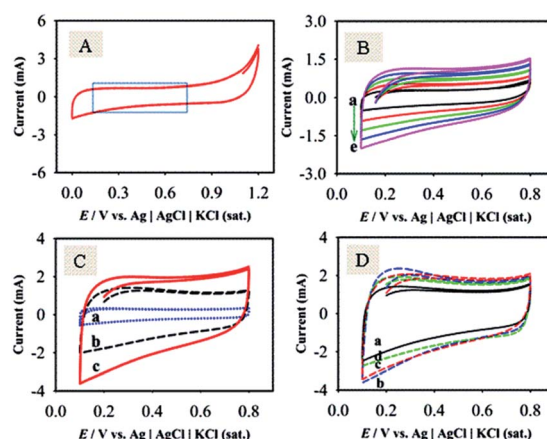

Fig. 3 XRD patterns of (a) GMCNT-5, (b) GMCNT-15, (c) GMCNT-30 and (d) GMCNT-50.

Fig. 5 CVs recorded for the GMCNT-15-modified electrode in the potential range from 0.0 to 1.2 V (A) at v of 10 mV s^{-1} and (B) in the potential range from 0.1 to 0.8 V at v of (a) 1, (b) 2, (c) 3, (d) 4 and (e) 5 mV s^{-1}. (C) CVs measured for (a) F-MWCNT, (b) GOM, (c) GMCNT-15 and (D) for (a) GMCNT-5, (b) GMCNT-10, (c) GMCNT-30, (d) GMCNT-50 composite-modified electrodes at v of 10 mVs^{-1}. The electrolyte solution was an aqueous 0.5 M Na_2SO_4 solution.

are about two- and four-times, respectively, lower than those for GMCNT-15. The CV responses of other composites prepared by varying % F-MWCNTs are compared in Fig. 5D. In addition, the effects of the amount of loading of GMCNT-15 on the CV response were also checked (see ESI†). In all cases, the rectangular shape of the CV response was obtained. However, this potential range chosen was employed for GCD measurements for determining C_{sp} quantitatively.

Fig. 6 shows GCD responses measured by applying constant current densities ranging from 0.5 to 20 A g^{-1}. The observation of the symmetrical GCD response demonstrates a high reversibility between the charging and discharging processes, as observed in the case of CV studies. The increasing current density shortens the charging time as a consequence of a lower degree of alignment/insertion of solvated Na$^+$ ions at/into the surfaces of materials forming a double layer. Ideally a longer charging time allows a high degree of insertion of solvated ions in the pore of the material, thus forming a rigid double layer.[56] The discharging time of the GCD response was used to calculate the C_{sp} as compared in Fig. 7.

Fig. 7 illustrates the comparison of the experimental values of C_{sp} for F-MWCNTs, GOM and GMCNTs with the theoretical value of α-MnO$_2$. At a glance, GMCNT-15 exhibited an excellent supercapacitive behaviour with the C_{sp} of 1380 F g^{-1}. With the increasing amount of F-MWCNTs in the ternary composite, C_{sp} increased initially and then decreased owing to a further increase in the % F-MWCNTs. It is rather interesting to note that C_{sp} varies in a convex parabolic fashion against the feed amount of F-MWCNTs. The C_{sp} of individual F-MWCNT is excessively low,[26] while that of GOM binary composites was 400 F g^{-1} in agreement with literature.[33] The combination of GOM and 5% F-MWCNTs in the GMCNT composite slightly enhanced C_{sp} to 420 F g^{-1}. An increase in C_{sp} was observed by increasing the percentage of F-MWCNTs up to 15% and then C_{sp} showed a decreasing trend in against further increase in F-MWCNTs. C_{sp} decreased with an increase in the current density applied for the GCD measurement and the amount of material loaded (see ESI†). This decrease in C_{sp} is due to the scarcity of the effective contact between the active surface on the electrode and electrolyte ion.[56]

The underlying reasons associated with frontier C_{sp} of MnO$_2$ obtained experimentally can easily be explained by considering
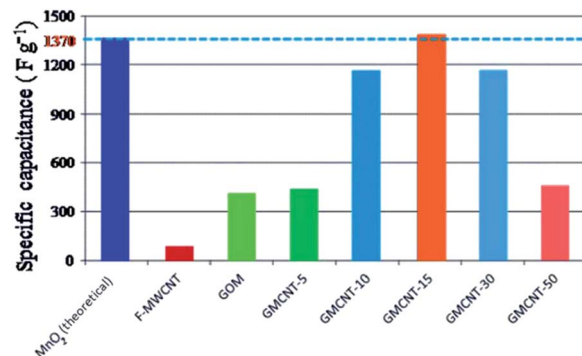
Fig. 7 Comparison of the specific capacitance of different materials under consideration. C_{sp} values of MnO$_2$ (theoretical),[13] MWCNTs[26] and GO[59] were taken from the literature.

the % MnO$_2$ present and the surface characteristics of GMCNT composites as described above. MWCNT itself provides a low C_{sp}, though it possesses a large surface area and high porosity. Pristine F-MWCNTs and GO show a purely double layer charging.[26,57] Conversely, the charging of MnO$_2$ involves a surface chemisorption of electrolyte ions, *i.e.*, Na$^+$ (eqn (1)), resulting in pseudo-capacitance. The charging-discharging cycle involves the rapid intercalation and de-intercalation of Na$^+$ ions, leading to the reduction and oxidation of MnO$_2$.[13] During charging-discharging, the conversion of Mn(III) to Mn(IV)[13,57] has been considered for graphene–MnO$_2$ (ref. 33) and GO–MnO$_2$ composites.[57]

$$MnO_2(s) + Na^+(aq) + e^- \rightleftharpoons MnOONa(s) \qquad (1)$$
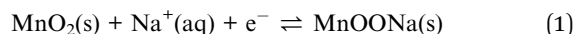
The extent of charging and hence C_{sp} generally depends on the amount of the accessible surface for the electrolyte ions and the amorphous nature of the oxide materials. The highly amorphous structure favours the electrolyte to insert into or to expel out from the oxide matrix.[58,59] On the contrary, the active surface area and ion-permeable porosity are the keys to regulate the ion accessible surface area. The size of hydrated ions of an aqueous electrolyte is in the range of 0.60–0.76 nm. Therefore, the micropores are not suitable for the insertion of hydrated ions due to the screening effect. However, the examination of data of % MnO$_2$ present that surface area, pore size, pore volume and degree of crystallinity GMCNT-15 possesses all the prerequisite features of an ideal supercapacitor material at their optimized levels. A moderate pore size (>2) nm is needed to maximize the electrical double layer capacitance by easy mobility and insertion of individual electrolyte ions into pores of the carbon electrodes.[59] However, the pores of more than 7 nm are not suitable for the adsorption of inserted ions since they loosely bind and hence do not form a compact double layer.[58,59] The surface of GMCNT-15 containing thin array of MnO$_2$ nanoparticles with suitable pores may function for the permeation of electrolyte ions in a lock and key manner that regulates enhanced effective ion diffusion *via* the nanostructure-top-on GO sheets for charging-discharging through the redox reaction, as shown in eqn (1).[57]
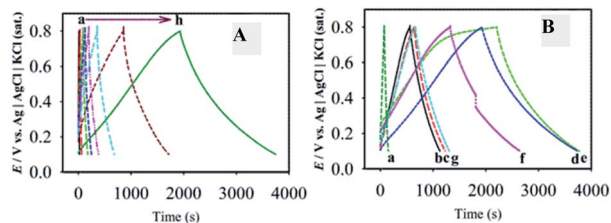

Fig. 6 (A) GCD responses of the GMCNT-15-modified electrode measured at current densities of (a) 20.0, (b) 10.0, (c) 5.0, (d) 4.0, (e) 3.0, (f) 2.0, (g) 1.0 and (h) 0.5 A g^{-1}. (B) GCD responses of (a) F-MWCNT, (b) GOM, (c) GMCNT-5, (d) GMCNT-10, (e) GMCNT-15, (f) GMCNT-30 and (g) GMCNT-50-modified electrode measured at 0.5 A g^{-1}.
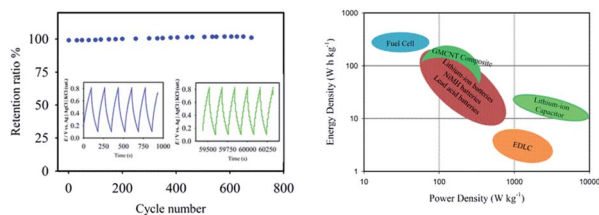
Fig. 8 Left panel: retention ratio as a function of cycle numbers for the GMCNT-15 composite. Inset shows the continuous GCD cycles: 1–5th (left) and 675–680th (right) cycles measured at 10 A g^{-1}. Right panel: Ragone plot.

The long-term cyclic stability of GMCNT-15 was tested for 700 cycles (Fig. 8). C_{sp} was found to increase with the cycle number. Cheng et al. have also observed this increase for MnO_2 and this process is known as electro-activation.[33] Upon continuous cycling, the GO sheets may move to adjust to different electrolyte ions.[33] The long-time charging-discharging may also help the ions access fully the sheets of GMCNTs to extract a full advantage of the surface area. The GMCNT-15 modified hybrid electrode exhibited a high energy density of 94.6 W h kg^{-1} and power density of 200 W kg^{-1} that are derived from the GCD measurement. The Ragone plot illustrated in Fig. 8 clearly shows that GMCNT-15 can store higher energy compared to lithium-ion batteries and supercapacitors, although being pseudocapacitive in nature, it possesses lower power density than a typical electric double layer capacitor.

4. Conclusions

α-MnO_2 can be well-dispersed using the 3D framework of MWCNTs horizontally dispersed on 2D GO nanosheets synthesized by a simple precipitation method. The synthesis involves a two-fold molecular engineering, wherein the in situ formation of α-MnO_2 and GO and the growth of the 3D MWCNTs/GO framework through the reaction between –OH groups of nascent GO formed instantly and –COOH groups of functionalized-MWCNTs added in a suspension containing graphite, $NaNO_3$ and $KMnO_4$ occur simultaneously under a strong acidic condition. The ternary composites of MnO_2/ MWCNT/GO are semi-crystalline and mesoporous in nature and the nano-flowers of MnO_2 distributed over 3D MWCNTs dispersed on GO frameworks. N_2 adsorption–desorption studies suggest that GMCNT-15 has an optimum surface area of 14 m^2 g^{-1} with a pore diameter of 2.55 nm. The MnO_2/MWCNT/GO composite-modified graphite electrode showed an outstanding supercapacitive behaviour in an aqueous Na_2SO_4 solution studied by cyclic voltammetry and chronopotentiometry. The maximum C_{sp} of 1380 F g^{-1} was obtained using an optimum amount of MnO_2 and MWCNTs in the composites, which is slightly higher than the theoretical C_{sp} of MnO_2. The corresponding values of energy density and power density are 94.6 W h kg^{-1} and 200 W kg^{-1}, respectively. The electrode fabricated was cycled for 700 cycles and interestingly C_{sp} increased with an increase in the number of cycles. Thus,

these composites can be practically used for fabricating low-cost, high-performance supercapacitor devices.

Conflicts of interest

There are no conflicts to declare.

Acknowledgements

References

1 H. Hwang, D. Shin, T. Kim, S. Park, T. Yeo and W. Choi, *J. Mater. Chem. A*, 2018, **6**, 22998–23009.

2 X. Lang, A. Hirata, T. Fujita and M. Chen, *Nat. Nanotechnol.*, 2011, **6**, 232–236.

3 K. Q. Ding, *J. Chin. Chem. Soc.*, 2008, **55**, 543–549.

4 T. Ohsaka, A.-N. Chowdhury, M. A. Rahman and M. M. Islam, *Trends in Polyaniline Research*, Nova Science Publishers, 2013, ISBN: 978-1-62808-427-6.

5 O. Sadak, W. Wang, J. Guan, A. K. Sundramoorthy and S. Gunasekaran, *ACS Appl. Nano Mater.*, 2019, **2**, 4386–4394.

6 K. Wen, G. Chen, F. Jiang, X. Zhou and J. Yang, *Int. J. Electrochem. Sci.*, 2014, **10**, 3859–3866.

7 Y. R. Ahn, M. Y. Song, S. M. Jo, C. R. Park and D. Y. Kim, *Nanotechnology*, 2006, **17**, 2865–2869.

8 U. M. Patil, R. R. Salunkhe, K. V. Gurav and C. D. Lokhande, *Appl. Surf. Sci.*, 2008, **255**, 2603–2607.

9 S. G. Kandalkar, J. L. Gunjakar and C. D. Lokhande, *Appl. Surf. Sci.*, 2008, **254**, 5540–5544.

10 A. González, E. Goikolea, J. A. Barrena and R. Mysyk, *Renewable Sustainable Energy Rev.*, 2016, **58**, 1189–1206.

11 K. Sun, C. A. Riedel, A. Urbani, M. Simeoni, S. Mengali, M. Zalkovskij, B. Bilenberg, C. H. De Groot and O. L. Muskens, *ACS Photonics*, 2018, **5**, 2280–2286.

12 X. Lang, A. Hirata, T. Fujita and M. Chen, *Nat. Nanotechnol.*, 2011, **6**, 232–236.

13 M. Toupin, T. Brousse and D. Bélanger, *Chem. Mater.*, 2004, **16**, 3184–3190.

14 M. Zhi, C. Xiang, J. Li, M. Li and N. Wu, *Nanoscale*, 2013, **5**, 72–88.

15 M. Huang, F. Li, F. Dong, Y. X. Zhang and L. L. Zhang, *J. Mater. Chem. A*, 2015, **3**, 21380–21423.

16 H. Y. Lee and J. B. Goodenough, *J. Solid State Chem.*, 1999, **144**, 220–223.

17 B. Wang, J. Park, C. Wang, H. Ahn and G. Wang, *Electrochim. Acta*, 2010, **55**, 6812–6817.

18 H. S. Roy, M. M. Islam, M. Y. A. Mollah and M. A. B. H. Susan, *Mater. Today: Proc.*, 2020, **29**, 1013–1019.

19 M. G. Rabbani, M. M. Islam, M. Y. A. Mollah and M. A. B. H. Susan, *Mater. Today: Proc.*, 2020, 1192–1198.

20 Y. Huang, J. Lu, S. Kang, D. Weng, L. Han and Y. Wang, *Int. J. Electrochem. Sci.*, 2019, **14**, 9298–9310.

21 Y. Ge, X. Wang and T. Zhao, *Front. Chem.*, 2019, **7**, 1–6.

22 K. Wen, G. Chen, F. Jiang, X. Zhou and J. Yang, *Int. J. Electrochem. Sci.*, 2014, **10**, 3859–3866.

23 C. J. Hung, P. Lin and T. Y. Tseng, *J. Power Sources*, 2014, **259**, 145–153.

24 H. Jia, Y. Cai, X. Zheng, J. Lin, H. Liang, J. Qi, J. Cao, J. Feng and W. Fei, *ACS Appl. Mater. Interfaces*, 2018, **10**, 38963–38969.

25 E. Grądzka and K. Winkler, in *Carbon Nanotubes - Recent Progress*, 2018.

26 F. R. Galvan, V. Barranco, J. C. Galvan and S. Batlle, *Sebastian Feliu Fajardo and García*, Intech, 2016, vol. i, p. 13.

27 L. Deng, Z. Hao, J. Wang, G. Zhu, L. Kang, Z. H. Liu, Z. Yang and Z. Wang, *Electrochim. Acta*, 2013, **89**, 191–198.

28 W. Chen, Z. Fan, L. Gu, X. Bao and C. Wang, *Chem. Commun.*, 2010, **46**, 3905–3907.

29 D. R. Dreyer, S. Park, C. W. Bielawski and R. S. Ruoff, *Chem. Soc. Rev.*, 2010, **39**, 228–240.

30 S. H. Aboutalebi, A. T. Chidembo, M. Salari, K. Konstantinov, D. Wexler, H. Kun Liu and S. Xue Dou, *Energy Environ. Sci.*, 2011, **4**, 1855–1865.

31 S. Mallakpour and S. Soltanian, *RSC Adv.*, 2016, **6**, 109916–109935.

32 Y. Wang, J. Wu and F. Wei, *Carbon*, 2003, **41**, 2939–2948.

33 Q. Cheng, J. Tang, J. Ma, H. Zhang, N. Shinya and L. C. Qin, *Carbon*, 2011, **49**, 2917–2925.

34 M. J. Rahman and T. Mieno, *J. Nanomater.*, 2014, **2014**, 1–9.

35 D. S. Ahmed, A. J. Haider and M. R. Mohammad, *Energy Procedia*, 2013, **36**, 1111–1118.

36 L. Stobinski, B. Lesiak, L. Kövér, J. Tóth, S. Biniak, G. Trykowski and J. Judek, *J. Alloys Compd.*, 2010, **501**, 77–84.

37 D. S. Ahmed, A. J. Haider and M. R. Mohammad, *Energy Procedia*, 2013, **36**, 1111–1118.

38 J. D. Núñez, A. M. Benito, S. Rouzière, P. Launois, R. Arenal, P. M. Ajayan and W. K. Maser, *Chem. Sci.*, 2017, **8**, 4987–4995.

39 D. P. Dubal, D. S. Dhawale, R. R. Salunkhe and C. D. Lokhande, *J. Electrochem. Soc.*, 2010, **157**, A812.

40 C. M. Julien, M. Massot and C. Poinsignon, *Spectrochim. Acta, Part A*, 2004, **60**, 689–700.

41 S. Devaraj and N. Munichandraiah, *J. Phys. Chem. C*, 2008, **112**, 4406–4417.

42 D. C. Marcano, D. V. Kosynkin, J. M. Berlin, A. Sinitskii, Z. Sun, A. Slesarev, L. B. Alemany, W. Lu and J. M. Tour, *ACS Nano*, 2010, **4**, 4806–4814.

43 S. Sadhukhan, T. K. Ghosh, D. Rana, I. Roy, A. Bhattacharyya, G. Sarkar, M. Chakraborty and D. Chattopadhyay, *Mater. Res. Bull.*, 2016, **79**, 41–51.

44 A. Gharib, L. V. Fard, N. N. Pesyan and M. Roshani, *Chem. J.*, 2015, **1**, 151–158.

45 H. van Bekkum, H. M. A. Buurmans, B. M. Wepster and A. M. van Wijk, *Recl. Trav. Chim. Pays-Bas*, 1969, **88**, 301–306.

46 G. M. Florio, T. S. Zwier, E. M. Myshakin, K. D. Jordan and E. L. Sibert, *J. Chem. Phys.*, 2003, **118**, 1735–1746.

47 C. Emmeluth, M. A. Suhm and D. Luckhaus, *J. Chem. Phys.*, 2003, **118**, 2242–2255.

48 S. L. Chou, J. Z. Wang, S. Y. Chew, H. K. Liu and S. X. Dou, *Electrochem. Commun.*, 2008, **10**, 1724–1727.

49 R. Xu, X. Wang, D. Wang, K. Zhou and Y. Li, *J. Catal.*, 2006, **237**, 426–430.

50 H. W. Park, T. Kim, J. Huh, M. Kang, J. E. Lee and H. Yoon, *ACS Nano*, 2012, **6**, 7624–7633.

51 Z. S. Yan, J. Y. Long, Q. F. Zhou, Y. Gong and J. H. Lin, *Dalton Trans.*, 2018, **47**, 5390–5405.

52 D. P. Hashim, N. T. Narayanan, J. M. Romo-Herrera, D. A. Cullen, M. G. Hahm, P. Lezzi, J. R. Suttle, D. Kelkhoff, E. Muñoz-Sandoval, S. Ganguli, A. K. Roy, D. J. Smith, R. Vajtai, B. G. Sumpter, V. Meunier, H. Terrones, M. Terrones and P. M. Ajayan, *Sci. Rep.*, 2012, **2**, 1–8.

53 K. S. Kim and S. J. Park, *J. Electroanal. Chem.*, 2012, **673**, 58–64.

54 R. R. Salunkhe, K. Jang, S. W. Lee, S. Yu and H. Ahn, *J. Mater. Chem.*, 2012, **22**, 21630–21635.

55 R. K. Gupta, J. Candler, S. Palchoudhury, K. Ramasamy and B. K. Gupta, *Sci. Rep.*, 2015, **5**, 1–11.

56 C. J. Hung, P. Lin and T. Y. Tseng, *J. Power Sources*, 2013, **243**, 594–602.

57 M. Seredych and T. J. Bandosz, *J. Mater. Chem.*, 2012, **22**, 23525–23533.

58 I. Tanahashi, *J. Electrochem. Soc.*, 1990, **137**, 3052.

59 L. Liao and C. Pan, *Soft Nanosci. Lett.*, 2011, **01**, 16–23.